Graphical Abstract

MicroCrystalNet: An Efficient Convolutional Neural Network for Microcrystal Classification using Scanning Electron Microscope Petrography

Mohammed Yaqoob, Mohammed Ishaq, Mohammed Yusuf Ansari, Issac Sujay Anand John Jayachandran, Mohammed Hashim, Thomas Daniel Seers

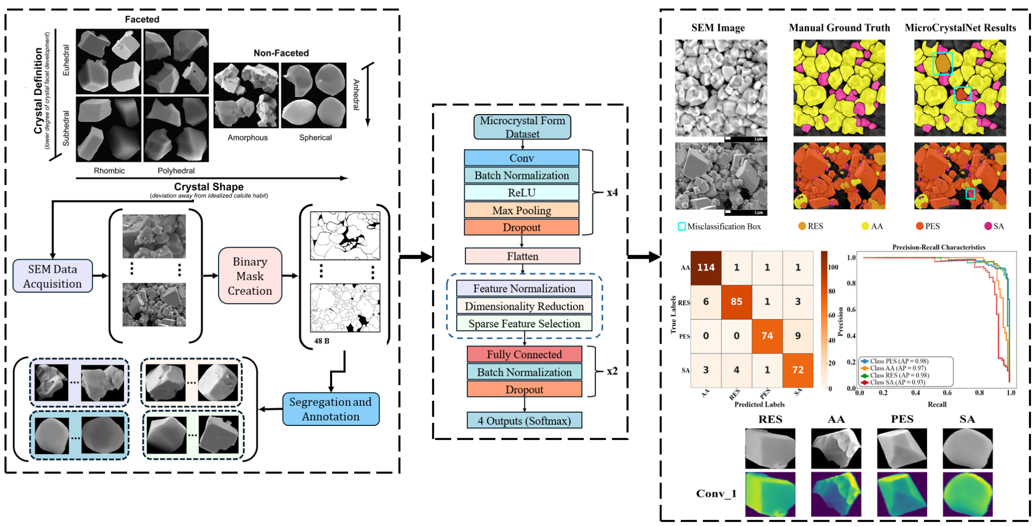

This is a pre-print version:

This manuscript has been submitted for publication in **MARINE AND PETROLEUM GEOLOGY**. Please note that, despite having undergone peer-review, the manuscript has yet to be formally accepted for publication. Subsequent versions of this manuscript may have slightly different content. If accepted, the final version of this manuscript will be available via the 'Peer-reviewed Publication DOI' link on the right-hand side of this webpage. Please feel free to contact any of the authors; we welcome feedback.

Highlights

MicroCrystalNet: An Efficient Convolutional Neural Network for Microcrystal Classification using Scanning Electron Microscope Petrography

Mohammed Yaqoob, Mohammed Ishaq, Mohammed Yusuf Ansari, Issac Sujay Anand John Jayachandran, Mohammed Hashim, Thomas Daniel Seers

- Deep learning segmentation-classification pipeline for SEM images of microcrystalline textures
- Lightweight Sparse Reduction Block CNN architecture promotes classifier Efficiency and Generalizability
- Tests using low-Mg calcites show excellent performance against benchmark classifiers
- Facilitates nanoscale automated / quantitative high volume microcrystal analytics

MicroCrystalNet: An Efficient Convolutional Neural Network for Microcrystal Classification using Scanning Electron Microscope Petrography

Mohammed Yaqoob[a,f], Mohammed Ishaq[a], Mohammed Yusuf Ansari[a,b], Issac Sujay Anand John Jayachandran[c,d], Mohammed Hashim[e], Thomas Daniel Seers[c]

[a]*Electrical and Computer Engineering, Texas A&M University at Qatar, Qatar Foundation, Doha, Qatar*
[b]*Electrical and Computer Engineering, Texas A&M University, College Station, College Station, 77843, TX, U.S.A*
[c]*Petroleum Engineering, Texas A&M University at Qatar, Qatar Foundation, Doha, 00000, Qatar*
[d]*Geology and Geophysics, Texas A&M University, College Station, College Station, 77843, TX, U.S.A*
[e]*Woods Hole Oceanographic Institution, 266 Woods Hole Road, Woods Hole, 02543-1050, MA, U.S.A*
[f]*Corresponding author email: yansari@tamu.edu*

Abstract

Morphological characterization of microcrystalline rock textures typically relies upon the visual interpretation and manual measurement of scanning electron microscopy (SEM) imagery: a practice fraught with subjectivity, inefficiency, sampling bias, and data loss. We introduce a state-of-the-art computer vision pipeline, built on deep learning architectures, for segmenting and classifying individual microcrystals from SEM images. Initially applied to low-Mg calcite carbonate rocks, instance segmentation is achieved using a custom-tuned version of Meta's Segment Anything Model (SAM). To train and test the classifier, we utilized 48 SEM images of diverse carbonate microtextures composed of Low-Mg calcite from studies performed worldwide. Each individual microcrystal (1852 in total) was labelled according to a bipartite classification scheme, encompassing both crystal shape (rhombic, polyhedral, amorphous, and spherical), and degree of crystal facet definition (euhedral to subhedral, anhedral), with a total of four distinct classes. MicroCrystalNet: our proposed classification model employs a convolutional neural network architecture, incorporating advanced feature map processing (feature normalization, dimensionality reduction, and sparse feature selection), integrated within a novel Normalized Sparse Reduction block. Performance metrics reveals excellent Average Precision scores (AP = 0.93-0.98) and Area Under Receiver-Operator Curve values (AUC = 0.95-0.99) across all classes, with visual comparison to manual ground truth images demonstrating powerful inter-class discriminatory power, even in the presence of occlusions.

This study establishes a baseline for the automated classification of microcrystalline rock textures. Leveraging SEM imagery and our high-throughput segmentation and classification framework, we enable quantitative characterization of microcrystalline geologic media. For instance, MicroCrystalNet can analyze microporous carbonate rocks at scale, revealing spatiotemporal trends in microporosity and diagenesis. To support reproducibility and further research, we provide the labeled dataset, feature extraction tool, and deep learning-based pipeline as open-source resources. This framework can be extended to other lithologies or non-geologic microcrystalline materials with the addition of specific training images and labels.

Keywords: SEM, petrography, microcrystalline calcite, carbonate characterization, deep learning, segmentation, classification

---

1. Introduction

Microcrystalline textures form common components of many lithologies, being prominent in the study of volcanic products (e.g. Wohletz (1983); Lautze et al. (2012); Deardorff and Cashman (2017)), ore deposit genesis and processing (e.g., Egglseder et al. (2019); Weng et al. (2017)), metamorphic textures (Ogasawara (2005); Stripp et al. (2006)), sandstone paragenesis (e.g., French and Worden (2013)), and the characterization of microporous carbonate rocks (e.g., Cantrell et al. (1999); Kaczmarek et al. (2015)). A unifying factor in this broad spectrum of lithotypes and problem domains is the de facto application of scanning electron microscopy (SEM) towards the study of microcrystalline textures (see the references above), with the advent of low cost benchtop SEM instruments making such analysis increasingly accessible (e.g., Cao et al. (2018)). The quantitative characterization of microcrystalline textures using SEM petrographic images remains, however, challenging. In many applications, SEM images present the rough topography of microcrystalline surfaces and crystal facets, unless specialized section preparation is undertaken (i.e., via high precision mechanical or broad ion beam polishing: French and Worden (2013); Smodej et al. (2019); Norbisrath et al. (2015)). Thus, individual microcrystals often suffer occlusions from the surrounding matrix, with the overall scene being subject to perspective effects, meaning that crystal shape, size and packing can only be resolved as 'apparent' properties. Within porous microcrystalline geologic media (e.g., microporous carbonate rocks), inter-crystalline void spaces visible in SEM micrographs suffer similar occlusions and artifacts (e.g., the presence of 'pore backs': Norbisrath et al. (2015)) making the evaluation of porous media properties challenging. Critically, the topographic surfaces of roughly cleaved microcrystalline matrix which have been the stalwart of microtextural characterization studies in multiple lithologies for decades largely preclude the application of automated image processing workflows (i.e., segmentation of material phases, proceeded by pore and/or particle labelling and property extraction), which have been leveraged to elicit a rich suite of rock physical properties from x-ray microtomographic volume images of macroporous media (e.g., mineral distributions, porosity, pore and particle size distributions, capillary pressure, single phase and relative permeability, fluid saturation distributions, wettability, thermal conductivity, elastic modulus etc.: e.g., Guntoro et al. (2019); Andrä et al. (2013); Andrew et al. (2014);Gao et al. (2020)). Fundamentally, the grayscale values in SEM micrographs represent emitted, scattered and backscattered electron signal intensity, which is influenced by multifarious factors, such as working distance, material composition, sample surface and/or crystallographic orientation and instrument settings (see Zhong et al. (2021)), correlating weakly with material phases or separable objects. Classic image processing approaches, such as gradient-based histogram thresholding, automated thresholding (e.g., Otsu et al. (1975)) and marker-based watershed transform are unable to produce meaningful segmentations of material phases or object labels from SEM micrographs of roughly prepared microcrystalline surfaces. Though this has not entirely deterred attempts at such analyses (e.g., Jouini et al. (2011)), the vast majority studies have employed manual crystallometry on the image plane (e.g., fitting polylines, annotations and masks) coupled with qualitative descriptions of crystal morphology.

The paucity of low user-intervention, high throughput image processing tools for the extraction of meaningful rock physical properties from SEM micrographs has severely curtailed the utility of this ubiquitous imaging modality in microcrystalline rock characterization. Major advances in instance segmentation and object classification in adjacent fields leveraging deep architectures (e.g., Jacobs (2022); Fan et al. (2023); Hörst et al. (2024)) do, however, offer considerable promise. For example, highly generalizable segmentation pipelines harnessing vision transformer (ViT) image encoders have been successfully applied towards the localization and instance segmentation of nuanced objects in complex scenes, targeting a broad range of image modalities and applications (e.g., Chen et al. (2021); Yang et al. (2022)). These developments have culminated in the advent of true one-shot segmentation (e.g., Kirillov et al. (2023)), offering the capacity to generate accurate object masks for previously unencountered segmentation tasks with minimal tuning. Further to this, the proliferation of Convolutional Neural Network (CNN) classifiers have revolutionized object classification tasks from image datasets (e.g., Sharma et al. (2018); Zhang et al. (2019); Ansari et al. (2021); Sutha et al. (2020)), with the enhanced capabilities to establish feature-to-class correlations providing unprecedented performance in determining inter-class separation.

Initially deployed towards the characterization of Low-Mg calcite carbonate rock textures, herein we leverage developments in deep learning and computer vision to develop a self-contained automated SEM image processing pipeline for the extraction and classification of microcrystals from SEM micrographs of rough cut rock chips. Specifically, we achieve zero-shot instance segmentation of individual microcrystals using a custom tuned implementation of Meta's Segment Anything Model (SAM Kirillov et al. (2023)), enabling SEM microtextural datsets to be interrogated for apparent microcrystalline properties (e.g., apparent crystal size, aspect ratio etc.). Further to this, we have implemented a bespoke CNN microcrystal classifier trained using 48 high resolution SEM images of Low-Mg calcite carbonate microtextures, comprising 1852 extracted microcrystals. We have annotated this dataset according to a bipartite classification scheme, encompassing both crystal shape (rhombic, polyhedral, amorphous, and spherical), and degree of crystal facet definition (euhedral to subhedral, anhedral). In the following sections we will present conceptual aspects of microcrystalline calcite characterization, crystallometry and classification in the context of the presented pipeline, prior to detailing its practical implementation, including training data selection, preprocessing and CNN model architecture. We then conduct a series of performance experiments using the proposed model, as well as a robust benchmarking exercise against state-of-the-art CNN image classification frameworks. Finally, the implications of our automated image segmentation and classification pipeline towards the quantitative characterization of microporous carbonate rocks, as well as broader applications towards other microcrystalline geologic media are also discussed.

1.1. Microcrystalline Carbonate Rock Characterization

Microporosity (i.e., pores with diameters of < 10 µm) is typically major component of carbonate rock pore systems, often being the dominant mode, and thus constitutes one of the most significant repositories of geofluids within the upper crust. Characterizing microporosity is therefore an essential endeavor for subsurface applications targeting carbonate lithologies, such as reservoir development, aquifer management, the geologic sequestration of carbon dioxide, and nascent subsurface energy storage (e.g., hydrogen). In limestones composed of low-Mg calcite (LMC), which are commonly encountered in ancient carbonate sedimentary rocks, micropores are typically hosted as interparticle pore systems bounded by microcrystals with a maximum diameter 10 µm (Hashim and Kaczmarek (2019)). As a consequence, it can be inferred that the morphology of calcite microcrystals directly controls key pore-scale (geometric) properties of the microporous domain (e.g., pore body size and shape, connectivity, tortuosity and pore throat radius) which govern rock physical properties such as porosity, permeability and capillary pressure measured at the continuum scale (Lambert et al. (2006); de Periere et al. (2011); Regnet et al. (2015, 2019); Kaczmarek et al. (2015); Hashim and Kaczmarek (2019)). Further to this, microcrystals can act as an archive of the paragenetic phases a given rock unit has undergone, which may otherwise remain obtuse from petrographic or geochemical analysis (Hashim (2022); Hashim and Kaczmarek (2020)).

Despite their significance towards carbonate diagenesis and petrophysics, the quantitative characterization of microcrystalline calcite remains challenging. Classically, the presence of microporosity inferred from the presence of 'blue haze' within optical petrographic images (Cantrell et al. (1999)), which results from subpixel averaging between calcite microcrystals and blue epoxy resin impregnated into the pore system (i.e., partial area effect: Trujillo-Pino et al. (2013)). Moreover, microporosity can be identified indirectly by the presence of high capillary entry pressure modes from mercury injection capillary pressure experiments (Sok et al. (2010)) and nuclear magnetic resonance (NMR) T_2 relaxation time distributions (Vincent et al. (2011)). Such indirect methods are however, are fraught with ambiguity and preclude linkage between the textural properties of microcrystalline calcite and their petrophysical signatures obtained from lab-based measurements.

In the context of macroporous geologic media, the advent of volume imaging techniques, and in particular x-ray microcomputed tomography (µCT) have revolutionized the study of pore systems, as well as the textural and mineralogical properties of their host frameworks (e.g. Siddique et al. (2023); Godinho et al. (2023); Kong et al. (2019)). Nanometric volume imaging techniques, such as nano-computed tomography (nCT: e.g., Puskarczyk et al. (2018)), focused ion beam scanning electron microscopy (FIB-SEM: e.g., Vilcáez et al. (2017)) and confocal laser scanning microscopy (e.g., Hassan et al. (2019)), suitable for the characterization of microporosity and/or microcrystalline calcite textures remains non-routine. Such methods require highly specialized and/or expensive instrumentation (esp., nCT), and are typically associated with challenging sample preparation and imaging protocols, resulting in prohibitively low throughputs and volumes of interest for the routine characterization of microporous carbonate rocks. Consequently, scanning electron microscopy (SEM) of broken surfaces of cuttings and rock chips is the de facto imaging technique for the characterization of microcrystalline carbonate rocks, in a practice dating back to the 1960s (Folk (1965); Mathews (1966); Longman and Mench (1978); Gischler and Erkoç (2013); Milliken and Curtis (2016); Hashim and Kaczmarek (2019)).

1.2. SEM Microcrystalline Calcite Morphometry

Herein, we utilize the term microcrystals (see Kaczmarek et al. (2015)) as opposed to alternate nomenclature in the literature, such as micrite (itself a portmanteau of 'microcrystalline' and 'calcite') and microspar (Folk (1965); Hashim and Kaczmarek (2019)), to avoid the genetic and scaling connotations such naming conventions carry. The main form of microporosity in ancient carbonate rocks which form the dominant focus of microcrystalline calcite characterization studies are interparticle pore systems bound within low-Mg calcite (LMC) microcrystals. Consequently, we focus our image segmentation and classification pipeline on this lithology, though it is readily extendable to additional carbonate microporous lithologies (i.e., dolomites, aragonites, high-Mg calcite etc.). Several studies have indicated that the morphology of the microcrystals and their packing arrangement have a direct impact on flow characteristics of microporous-dominated pore systems (Lambert et al. (2006); de Periere et al. (2011); Regnet et al. (2015, 2019);

Hashim and Kaczmarek (2019)), leading to the significant activity within the field.

Microcrystal morphometry involves characterization of the size and morphology of the microcrystals. However, only size is universally measured as it is intuitive and trivial to quantify from SEM microtextural image datasets (Lambert et al. (2006); de Periere et al. (2011); Kaczmarek et al. (2015); Hashim (2022)). Indeed microcrystal size has been used to evidence a number of stabilization hypotheses, including aggrading neomorphism (Folk (1965); Folk and Robles (1964)), Ostwald ripening (including hybrid Ostwald ripening: Richard et al. (2007); Carpentier et al. (2015); Morad et al. (2018)) and the purely diagenetic origin of calcite crystals (Steinen (1979, 1982); Kaczmarek et al. (2015); Hasiuk et al. (2016); Hashim and Kaczmarek (2019, 2020, 2021); Hashim (2022)). Most studies equate microcrystal size to the major crystal axis length, though this can only be considered as apparent size in the context of SEM micrograph datasets due to presence of occlusions and non-optimal crystal alignment with the electron optical axis. Despite these challenges, the use of apparent crystal major axis length as a proxy for size has proved to be popular in the literature (see Table 1 in de Periere et al. (2011)). In practice, this typically entails the arbitrary selection of crystals from the image, with the use of manual measurements (i.e., in the older literature) or CAD primitives in image processing software tools (e.g., ImageJ, JMicroVision: Roduit et al. (2007), Schindelin et al. (2015)) to measure crystal size. As a consequence, studies typically provide size ranges for a limited number of microcrystals, and do not specify protocols to mitigate subjectivity or sampling bias, thereby implying the stated size ranges are operator-specific. While this subjectivity has been mostly borne out of necessity, due to the lack of automated object localization and segmentation tools for SEM microcrytalline datasets, such studies have limited utility in drawing robust statistical inferences on microcrystalline size due to the inherent uncertainties they carry (Blott and Pye (2008); Hryciw et al. (2016); Anusree and Latha (2023)).

In contrast to crystal size, the quantification of microcrystalline calcite crystal morphology from SEM petrographic datasets is non-trivial. As a consequence, workers have tended to qualify calcite microcrystal geometry using terminology laid out by Friedman (Friedman (1965)), which itself was appropriated from igneous petrology literature. In this regard, the terms euhedral, subhedral and anhedral refer to crystals with well-defined, moderately defined and poorly defined crystal faces respectively (Figure 1). In this work, we make a distinction between the descriptors of microcrystal definition above, which describe the degree of calcite crystal facet development, as per Friedman's scheme (Friedman (1965)), and calcite microcrystal shape, which corresponds more closely to the expression of calcite crystal habit (or lack thereof). Calcite microcrystal shape describes how many facets a given crystal contains, and comprises two overarching classes (faceted and non-faceted). Faceted microcrystals can be assigned to one of two subclasses, namely rhombic crystals with six faces (i.e., corresponding to perfect rhombohedral habit) and and polyhedral crystals with more than six facets (i.e., scalenohedral, prismatic, tabular habit etc.). Non-faceted microcrystals have no discernible crystal faces, and can fall into amorphous (no discernible form) and spherical (also referred to as rounded) subclasses (see Figure 1). Whilst not widely quantified within the literature, crystal shape and definition arguably hold more prominent roles in the field of microporous carbonate rock characterization when compared to crystal size, being key diagnostic parameters in most calcite microcrystal classification schemes. For example, all texture classification schema, with the exception of (Moshier (1989)), explicitly define shape as a major textural component (Hashim and Kaczmarek (2020)). Additionally, these metrics have been extensively used to infer the formative environments and diagenetic processes that give rise to natural microcrystalline calcite textures, as well as track the effects of experimental controls in empirical crystal synthesis studies. For example, it has been proposed that rhombic and polyhedral crystals are indicative of 'clean' versus 'dirty' growth respectively, potentially corresponding to calcite precipitation in the presence of ion-depleted (e.g., freshwater) and ionic-rich (e.g., brine) subaqueous environments (Hashim (2022)). Alternately, crystal definition has been widely used to evidence both late-stage dissolution (e.g. Lambert et al. (2006); Tavakoli and Jamalian (2018); Valencia and Laya (2020)) and abiotic / microbial precipitation (e.g., Morad et al. (2018); Ehrenberg et al. (2012); Kaczmarek et al. (2015); Hashim and Kaczmarek (2020)).

Despite the tendency for geological literature to often treat these terms interchangeably, crystal shape and definition are fundamentally different descriptors of calcite microcrystal morphology (e.g., there are examples of rhombic crystals with both well-defined and poorly defined facets). In an effort to harmonize and consolidate microcrystalline calcite morphology nomenclature, we propose a bipartite classification scheme, encompassing both microcrystal shape and definition (see Figure 1). For parsimony, we have combined euhedral and subhedral subclasses in our current implementa-

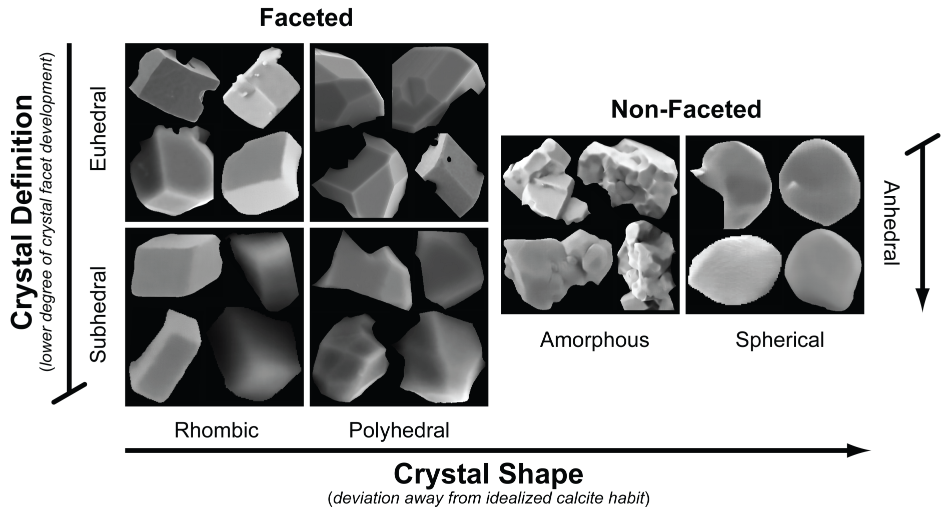

Figure 1: Classification scheme for calcite microcrystalline shape and form.

tion of MicroCrystalNet, resulting in a total of four classes observed in the training/tets dataset: namely, (1) Rhombic-Euhedral/Subhedral (RES), (2) Polyhedral-Euhedral/Subhedral (PES), (3) Amorphous-Anhedral (AA) and (4) Rounded-Anhedral (RA).

2. Proposed Dataset

We have collected and annotated a large-scale LMC microcrystalline calcite dataset (named hereafter lmcDB), which contains 1,852 annotated microcrystals extracted from 48 SEM images. In this section, we present the process of image acquisition and processing, as well as the properties of the proposed dataset.

2.1. Data Collection and Annotation

2.1.1. Data Collection

The scanning electron microscope (SEM) images utilized in this study were obtained at the Woods Hole Oceanographic Institution (WHOI), USA, using three instruments: namely JEOL 7500F, JEOL 6610LV, and JEOL IT100 series scanning electron microscopes. Imaging parameters were consistent across all samples, with an accelerating voltage of 20 kV and a working distance of 10 mm. To enhance image quality, samples were coated with either 10 nm of osmium, 30 nm of gold, or 30 nm of carbon. SEM images were captured at a resolution of 2048x2048 pixels, with a pixel size of 10 nanometers, ensuring individual calcite microcystals could be readily resolved. Raw SEM images contain noise and artifacts common in scanning electron imaging, which represent potential sources of error within the presented classification framework. Charging artifacts, caused by the accumulation of electrons on non-conductive samples, can lead to aberrations, with thermal drift, resulting from changes in temperature during imaging, causing grayscale shifts in the pixel intensity values of different images. Prolonged exposure to the electron beam can lead to beam damage, altering the sample's structure and introducing physical artifacts. Additionally, noise inherent to the SEM's detector can impact upon image quality, especially at higher magnifications. Consequently, an initial dataset of SEM micrographs were vetted for the presence of noise and aberrations which could prove deleterious to the performance of the classifier, resulting in a total of 48 high quality LMC calcite microtextural images forming the basis of the lmcDB dataset.

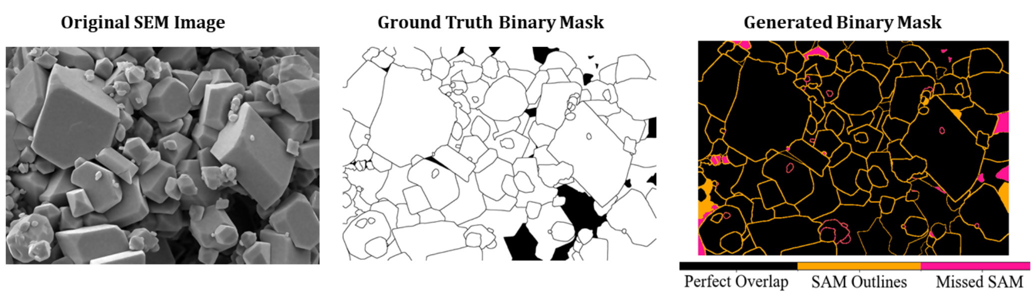

Figure 2: Comparison of Original SEM Images, Ground Truth Binary Masks, and Generated Binary Masks

The dataset includes two types of samples: natural and synthetic. Natural samples were sourced from Cretaceous aged deposits, namely the Lower Cretaceous Stuart City Trend, Texas, USA, and Thamama Group, UAE, as well as modern ooids from Ambergris Cay of the Turks and Caicos Islands (British Overseas Territory). Samples were prepared by breaking small chips from core material, gently pulverizing them using an agate mortar and pestle, with dry sieving used to obtain a size fraction of 90 to 202 µm. The sieved materials were then mounted, coated, and examined under the SEM. Synthetic samples consisted of calcite formed from aragonite during hydrothermal stabilization experiments. These experiments were performed in Teflon-lined stainless steel acid digestion vessels with controlled temperatures (50 to 200 ºC), fluid volumes to solid mass ratios (0.8 to 150 mL/g), and specific solution chemistries (DI and artificial seawater). Various reactants (single crystal aragonite, laboratory precipitated aragonite, corals, gastropods, calcifying algae) and sizes ($<$ 63 to 500 µm) were used, with experimental durations ranging from two to 83 days. Following the experiments, precipitated solids were separated from the fluids, washed with DI water, and dried in a vacuum desiccator at room temperature.

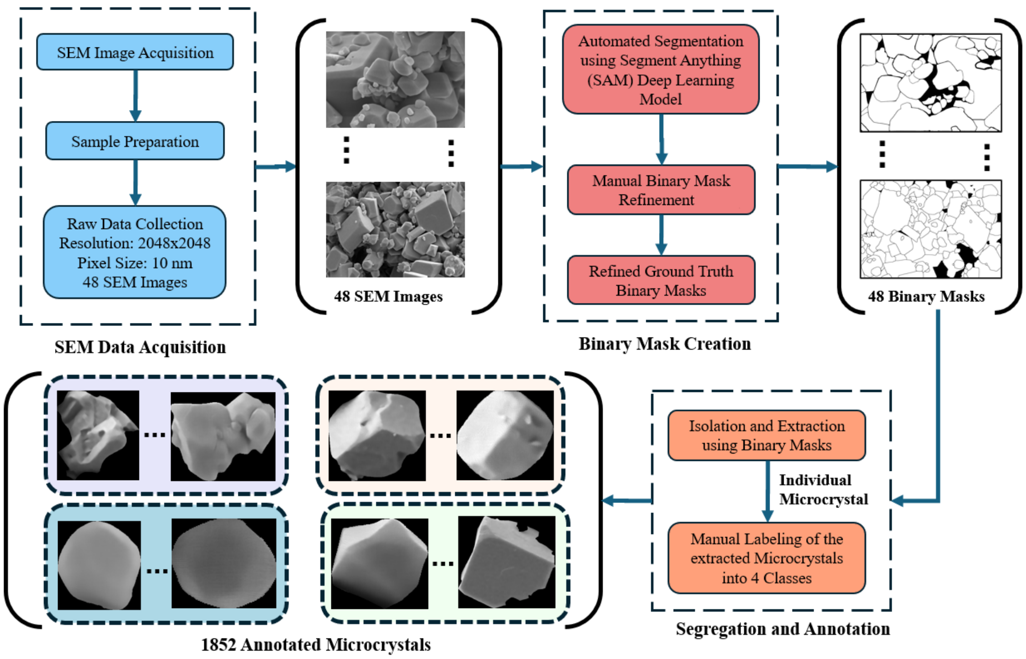

Figure 3: Image processing pipeline used for creation of lmcDB.

2.1.2. *Binary Mask Creation*

In this work, instance segmentation of individual calcite microcrystals from SEM images is achieved using a custom-tuned implementation of Meta's Segment Anything Model (SAM): a foundation model with zero-shot transfer learning capabilities. This fine-tuned SAM implementation isolates individual microcrystals via the generation of binary masks, providing high throughput segmentation of large SEM microtextural datasets, which form the prerequisite for deep learning-based microcrystal classification. Comparison with manually annotated ground truth data reveals a remarkable accuracy of 97.6% (see Figure 2), with the majority of non-overlapping areas relating to the disparity in the boarder thickness between our fine-tuned SAM and the manually annotated masks (see Figure 2). To ensure optimum accuracy of the lmcDB training dataset, manual corrections were performed to custom-SAM annotated masks in limited cases.

2.1.3. Microcrystal Labeling

Individual images in the lmcDB dataset contained an average of 40 microcrystals, ranging between 50 to 180 microcrystals per image dependant upon crystal size. The 1852 segmented microcrystals were stored as separate image files (tag image file: .tif) along with metadata describing sample provenance, image processing steps, and segmentation parameters. It should be noted that this segmented microcrystal dataset can be readily interrogated for microcrystal morphometric properties, such as apparent crystal size (in pixel units / real world units if the spatial resolution is known) and aspect ratio, though the analysis of such metrics are not the focus of the present study.

Microcrystal labeling was performed manually, with each microcrystal categorized using the scheme presented in Figure 1, based upon qualitative evaluation of its morphological features. A team of three experts conducted the labeling process to ensure accuracy and consistency. Despite this, the potential for subjective bias remained, with subjective interpretation by human operators offering disparities in the labelled dataset, highlighting the importance of a thorough and iterative labeling process to minimize errors and enhance the dataset's quality. Consequently, each segmented microcrystal was reviewed by at least two experts, and discrepancies were resolved through consensus. It should be noted that labeling and annotating microcrystals present in SEM images poses several challenges. Ambiguity in 2D projections and occlusions can make distinguishing between different shapes (e.g., RES, PES), challenging, potentially giving rise to misclassifications, introducing inconsistencies into the labels.

3. MicroCrystalNet Architecture

Convolutional Neural Networks have achieved state-of-the-art performance in several fields, including medical image analysis (Ansari et al. (2023b); Rai et al. (2023)), biomedical signal processing (Ansari et al. (2024, 2023a)), and drug discovery (Chandrasekar et al. (2023); Ansari et al. (2022)). Consequently, The proposed MicroCrystalNet is designed to leverage spatial and global features extracted by convolutional layers. The architecture incorporates advanced feature map processing, including feature normalization (Lee et al. (2019)), dimensionality reduction (Zhao and Du (2016)), and sparse feature selection (Huang and Wang (2018)), integrated within a novel Normalized Sparse Reduction (NSR) block (see Figure 4). The main stem of MicroCrystalNet comprises four sequential convolutional blocks, that serve as the primary feature extractors. Each block consists of a convolutional layer followed by batch normalization (Bjorck et al. (2018)), a Rectified Linear Unit (ReLU) (Agarap (2018)) activation function, max pooling, and dropout. The convolutional layers employ varying filter sizes (3x3, 5x5, and 7x7), providing a receptive field with sufficient coverage of crystal area bound within the input image patches. By placing Batch Normalization before the ReLU activation, the model stabilizes the learning process and accelerates training. This arrangement reduces internal covariate shift, ensuring that the input to each layer maintains a consistent distribution, which in turn aids in faster convergence and improves robustness. The ReLU activation function is then applied to introduce non-linearity, allowing the network to learn and represent complex non-linear patterns inherent within the data. Following ReLU, the max pooling operation with a factor of two is applied (Christlein et al. (2019)). Max pooling reduces the spatial dimensions of the feature maps while retaining the most relevant spatial features needed for final classification. The application of dropout after max pooling imbues regularization upon the network. Dropout prevents overfitting by randomly setting a fraction of the activations to zero during training, thereby preventing the network from relying on specific portions of feature maps (Baldi and Sadowski (2013)). Consequently, the convolutional block architecture facilitates feature extraction, stabilizes and accelerates learning, and improves generalization. The number of convolutional kernels increases progressively, starting from 32 and doubling at each subsequent block, culminating at 128 kernels.

The extracted feature map from the convolutional blocks is flattened to a vector and passed as an input to the NSR Block. This block introduces a series of operations aimed at enhancing microcrystal feature representation. The first stage within the NSR Block is feature normalization, performed using Z-score normalization (Cheadle et al. (2003)). This step standardizes pixel intensities to ensure to ensure coherant scaling. Normalization subdues

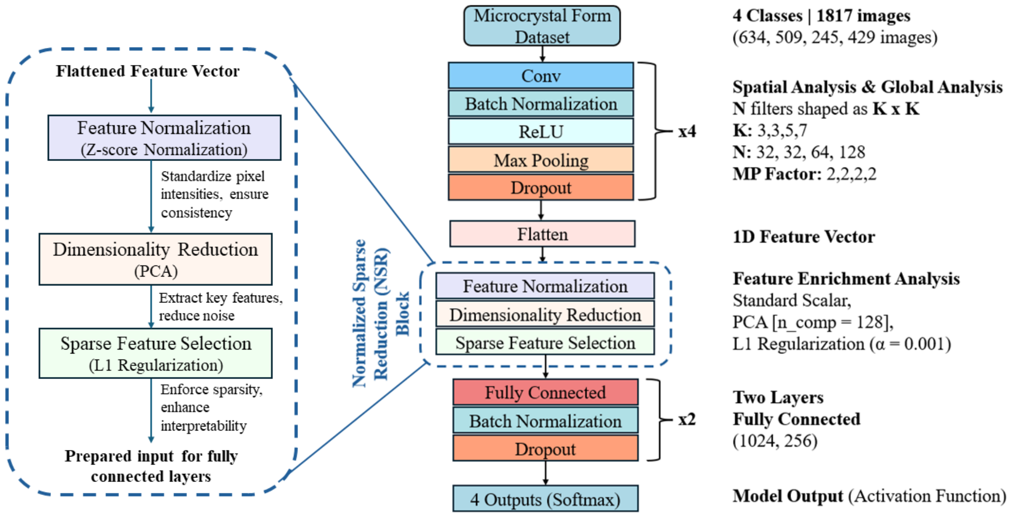

Figure 4: Proposed MicroCrystalNet architecture for microcrystal form classification.

the dominance of certain features due to scaling disparities, which enhances the learning efficacy of the successive fully connected layers. Following normalization, dimensionality reduction is applied through Principal Component Analysis (PCA) (Maćkiewicz and Ratajczak (1993)). This technique transforms the high-dimensional feature space into a lower-dimensional space by identifying the principal components that capture the majority of variance within the input data. By retaining only the most critical components, PCA reduces noise in the feature map whilst retaining the most significant features. This reduction not only simplifies the structure of the successive fully connected layers but also enhances its ability to generalize by focusing on essential patterns within the data. The final stage within the NSR Block involves sparse feature selection, implemented via L1 regularization. L1 regularization (Schmidt et al. (2007)) technique adds a penalty proportional to the absolute value of the feature weights, enforcing sparsity in the feature space. By promoting sparsity, L1 regularization helps in identifying and retaining only the most informative features while discarding less important ones. This focus on critical features enhances interpretability and ensures that the model concentrates on the most relevant aspects of the data, thereby improving classification performance. Altogether, the NSR block condenses the extracted feature map, minimizing the computational complexity within the fully connected layers, thereby improving efficiency. The transformed feature vector is then fed into a series of fully connected layers. The network comprises two fully connected layers with 1024 and 256 neurons, respectively. Batch normalization (Bjorck et al. (2018)) and dropout (Baldi and Sadowski (2013)) are applied to these layers to maintain training stability and prevent overfitting. The output layer employs a Softmax activation function, providing probabilistic predictions for each class.

4. Empirical Setup

4.1. Evaluation Metrics

We utilize a range of evaluation metrics to evaluate classification performance in our model experiments. Overall *accuracy* is measured as the ratio of correctly classified instances to the total number of instances, offering a general performance indicator. Additionally, *Top-1 Accuracy* gauges the proportion of instances where the highest probability prediction matches the true class label, whilst *Top-2 Accuracy* maps instances where the true class was amongst the top two highest probability predictions. Defined as the ratio of true positive predictions to the sum of true positive and false positive predictions, *Precision* indicates the model's ability to correctly identify positive instances. Measured as the ratio of true positive predictions to the sum of true positive and false negative predictions, *Recall / sensitivity* provides an indication of the model's capacity to capture all positive instances. Finally, the *F1 score*, which represents the harmonic mean of precision and recall, balances both false positives and false negatives, providing a holistic indicator of model performance. These metrics collectively provide a comprehensive evaluation of model performance, addressing both the accuracy of predictions and the effectiveness in identifying and capturing relevant instances of each class.

4.2. Data Preprocessing

Initially, the edge preserving non-Local Means (NLM) filter was applied was applied to images, resulting in a reduction in noise level of 30%, as measured by the signal-to-noise ratio (SNR: imrpovement of 10 dB to 16 dB). Further denoising was undertaken using Noise2void denoise package (Krull et al. (2019)) in Fiji, providing a SNR improvement of 19 dB. Subsequently, an unsharp masking was employed to enhance the edges of the microcrystals, which may have been perturbed by denoising operations. Unsharp mask enhances local contrast, making microcrystal boundaries more distinguishable, improving SNR to 22 dB. Next, Morphological operations, specifically opening and closing, were used to further refine the images. Morphological opening using a 5x5 structuring element was used to remove small spots from the images, reducing the background noise and improving SNR to 25 dB. The structuring element used for opening had a diameter of 5 pixels. Subsequently, morphological closing was applied to close small holes within the microcrystals, resulting in solid, contiguous crystal facets and thus optimum conditions for accurate segmentation.

4.3. Implementation Details

The experiments were executed in a high-performance workstation equipped with an AMD Ryzen Threadripper PRO 3995WX processor, featuring 64 cores and 128 logical processors, paired with 512 GB of memory. The models were implemented in Python 3.11 using the TensorFlow and Keras deep learning frameworks, with Python 3.11. Cross-validation was performed to ensure the robustness of the results.

MicroCrystalNet structure was finalized after an extensive hyperparameter optimization process, with experiments conducted using different configurations of layers, depths, regularization techniques, parameter choices, and activation functions. After identifying an efficient architecture, the model was further fine-tuned by testing various batch sizes (16, 32, 64, 128, and 256) and image resolutions (16x16, 32x32, 64x64, and 128x128). The model's generalization capability was determined with different dropout rates (0.2, 0.5, 0.7). The final model was trained using the Adam optimizer with a learning rate of 0.001, selected after comparative trials with other optimizers, such as Stochastic Gradient Descent (SGD) and RMSprop. Dropout layers with a dropout rate of 0.5 were used after fully connected layers to randomly deactivate neurons during training, reducing the risk of overfitting. The categorical cross-entropy loss function was used to measure the model's performance, which is suitable for multi-class classification tasks (Ho and Wookey (2019)). Training was conducted over 30 epochs with a batch size of 32, which was found to effectively balance training speed and model performance.

The training process of MicroCrystalNet used Learning Rate Scheduling, reducing the learning rate by a factor of 0.1 if the validation loss did not improve for five consecutive epochs. This allowed the model to take larger initial steps for optimization and then smaller steps as it approached convergence. Early Stopping was employed to halt training when the model's performance plateaued, preventing overfitting and conserving computational resources. Additionally, the model with the best performance during training was saved locally. The optimal data split ratio that yielded the best model results was 80% for training, 10% for validation, and 10% for testing. This distribution facilitated a robust evaluation of the model's generalization capabilities. The model's performance was further assessed using K-Fold Cross-Validation with a k value of 5, ensuring a robust evaluation of stability and reliability.

5. Results

This section presents the performance evaluation of MicroCrystalNet in classifying various microcrystal forms segmented from SEM petrographic images. It encompasses a description of the training procedure, an assessment of the model's accuracy for each individual microcrystal class, and visualizations of the deep network features using t-SNE. Furthermore, we offer insights into the explainability of the network's performance and present ablation studies aimed at fine-tuning the MicroCrystalNet model.

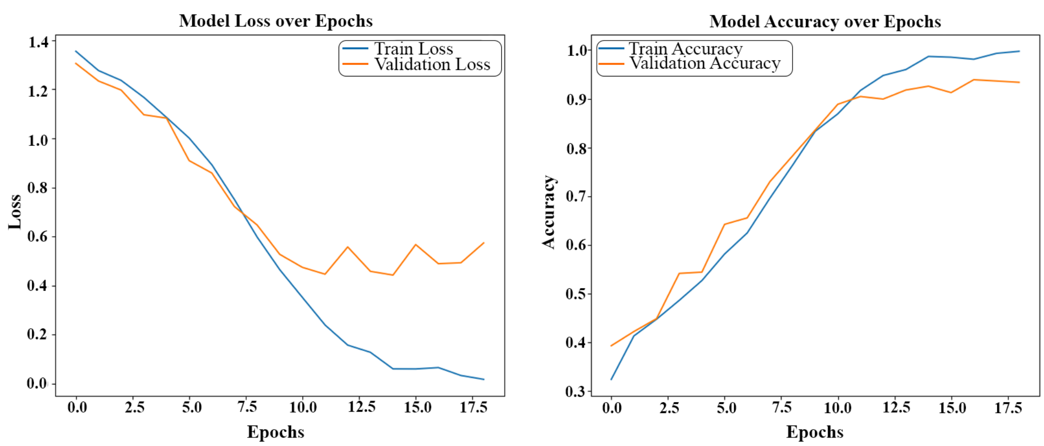

Figure 5: Training loss (left) and model accuracy (right) over epochs.

Loss curves and the evolution of model accuracy over epochs are presented in Figure 5, demonstrating a consistent decrease in train loss, signifying effective learning and concomitant error minimization on the training set. Figure 5 also provides insights into the model's learning progress and evidences model overfitting or underfitting. In this regard, validation loss plateaus after

10 epochs while the training loss continues to decrease, suggesting the initiation of the overfitting after the 10th epoch. The use of the Early Stopping procedure ensures that model training terminates if the validation loss fails to improve for several epochs. The accuracy plot shows an inverse relationship to the loss curves, which confirms the model's progressively improved classification performance. Notably, the training accuracy reaches nearly 98%, whilst the validation accuracy levels off just below 93%. The steady increase in validation accuracy indicates that the model is generalizing well to new data: a critical attribute of robust deep neural networks.

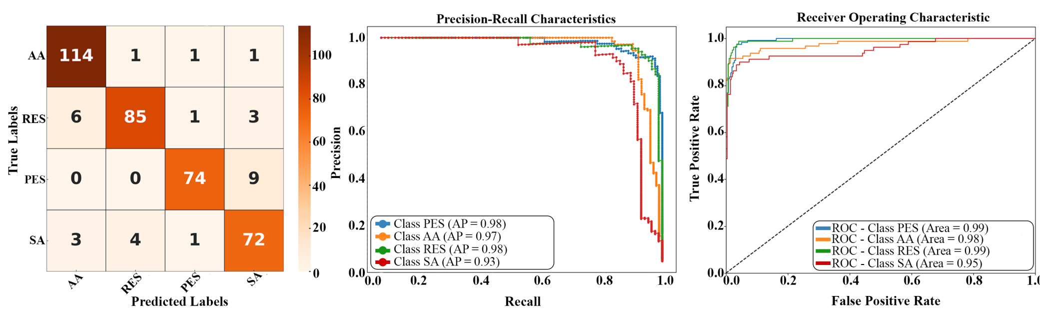

Figure 6: Confusion matrix (left), Precision-Recall curves (center), and ROC-AUC curves (right).

The confusion matrix, precision-recall curves, and ROC-AUC curves are presented together in Figure 6. The confusion matrix provides a detailed breakdown of the classification results, displaying the number of correct and incorrect predictions for each class, with high values along the diagonal indicating accurate classifications, whilst off-diagonal values highlighting misclassifications. Specifically, the matrix shows that the Polyhedral-Euhedral/Subhedral class suffers the most misclassifications, with notable confusion between the PES and Spherical-Anhedral classes, leading to nine instances of PES microcrystals being classified as SA. Additionally, six instances of the Rhombic-Euhedral/Subhedral class are predicted as Amorphous-Anhedral, evidencing apparent morphological overlap between the aforementioned classes.

The precision-recall curves illustrate the model's ability to handle class imbalances by displaying each class's trade-off between precision and recall. High precision and recall values across classes indicate that the model effectively identifies relevant instances and minimizes false positives. From the precision-recall curves, we observe that the model achieves high average precision (AP) scores for each class: RES (AP = 0.98), PES (AP = 0.98), AA (AP = 0.97), and SA (AP = 0.93). We note that the Spherical class has the lowest AP due to the comparatively high rate of False Positives and False Negatives encountered.

The ROC-AUC curves further evidence the model's performance by demonstrating the true positive rate against the false positive rate at various thresholds. High AUC values reflect strong discriminatory power between the classes. The ROC-AUC values are remarkably high across all classes: RES (AUC = 0.99), PES (AUC = 0.99), AA (AUC = 0.98), and SA (AUC = 0.95). indicating robust model performance, particularly in distinguishing PRES and RES classes, while the SA class, though slightly lower, still shows substantial discriminatory ability.

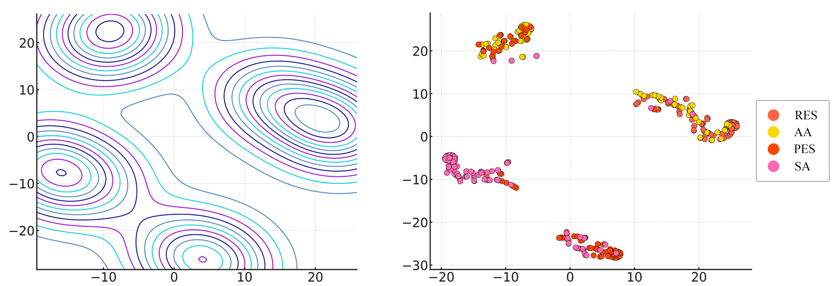

Figure 7: 2D t-SNE visualization of the lmcDB dataset (left), showing distinct class clusters with some overlap between the AA and SA classes, while the energy kernel (right) highlights point density and distribution.

t-distributed stochastic neighbor embedding (t-SNE) visualization of the lmcDB dataset reveals discrete clusters for each class, indicating that the model effectively captures the distinct morphometric features of each microcrystal class, evidencing the strong discriminatory power of the proposed model. There are, however, several instances of class overlap, particularly between AA and SA classes, indicating potential ambiguity / similarity between their feature sets, posing challenges to the classifier. This behavior conforms to the model's confusion matrix (see Figure 7), which revealed misclassifications between these two classes.

[0]The bottom image (00-215-1-3000X) is synthetic grown, and the top image (crls-215-2-5000X) is from coral. Both images exhibit granular euhedral textures as per Kaczmarek et al. (2015) but with mixed shapes. The images have not been previously published.

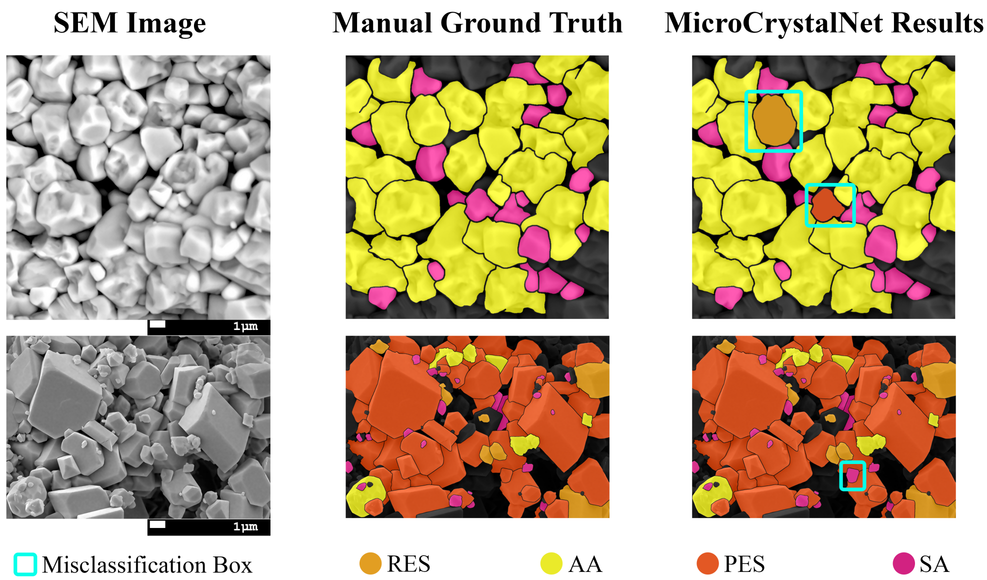

Figure 8: Visual comparison of classification results. Each instance includes the original microcrystal image (left), its manually labeled color map (center), and the MicroCrystalNet classified color map (right). Misclassifications are highlighted in teal boxes, with most errors occurring in the spherical class, reflecting evaluation metrics and confusion matrix findings.

Visual comparison between manually annotated ground truth images and MicroCrystalNet classified SEM micrographs further evidence the performance of the proposed model Figure 8, providing a tangible example of the model's precision and recall in a practical context. Notably, the model is able to closely match human operator perception, correctly classifying microcrystal objects even in cases where strong occlusions with the surrounding microcrystalline matrix occur. Despite this, some misclassifications can be identified, primarily occurring within the spherical class, aligning with observations from the previously computed evaluation metrics, confusion matrix analysis and t-SNE visualizations. Notwithstanding these minor discrepancies, this comparative analysis galvanizes MicroCrystalNet's potential as a powerful tool for high volume petrographic classification of microtextural image datasets, offering equivalent classification accuracy and many orders of magnitude improvement in throughput when compared to manual labeling.

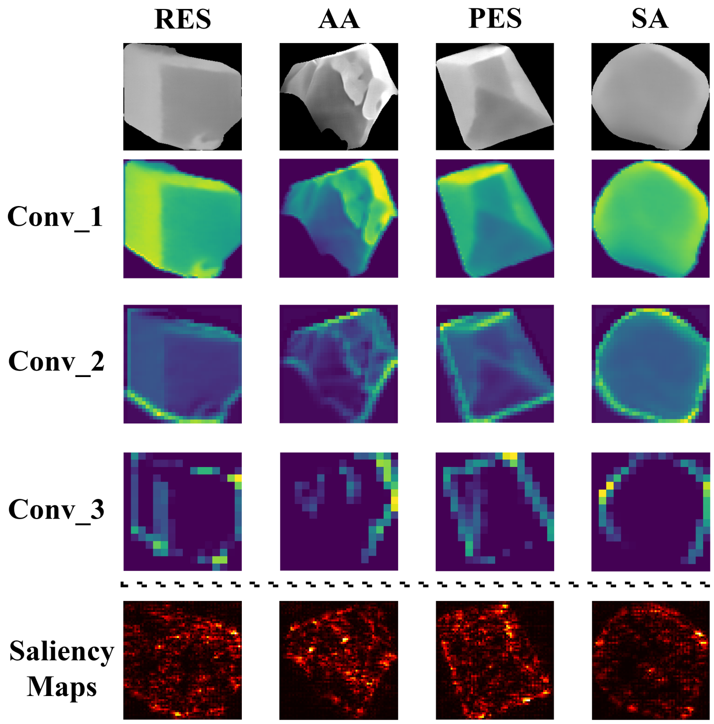

Figure 9: Interpretability and explainability tools: Activation maps (top) and saliency maps (bottom) for each of the four classes (RES, PES, AA, SA). Activation maps show the features captured by each convolutional layer, while saliency maps highlight regions with the highest impact on predictions.

5.1. Model Interpretability and Explainability

We utilize activation maps and saliency maps to aid the interpretability and explainability of the MicroCrystalNet model (Figure 9). Specifically, activation maps for each of the four convolutional layers in our model where generated for one representative image selected from each of the four classes, with accompanying saliency maps used to identify the most influential image regions for model predictions. Activation maps enable the features the model focuses on at different layers to be identified, with shallower layers capturing edges and textures, whilst deeper layers capture more complex patterns and shapes relevant to the classification task. Feature maps become progressively aliased within deeper layers due to the max-pooling operation, which reduces the spatial resolution. It is evident from the Conv_3 feature map that the network learns to extract crystal borders, utilizing them as the primary feature for classification. Conversely, saliency maps highlight the regions of the input image that have the highest impact upon classifier output, relating image regions to model predictive power. Saliency maps for all four classes reveal key structural features, such as crystal outlines, ridges, facets / surface curvature, and pits distinguish each class. For example, the model emphasizes the smooth, rounded edges in the SA class, whereas angular corners and flat surfaces are diagnostic of the PES class.

Combined, these visual tools enhance our understanding of the model's decision-making process, providing mechanistic insights into way MicroCrystalNet captures and utilizes relevant image features for accurate microcrystal morphometric classification. Transparency and interpretability are crucial for deploying deep learning models in practical applications, ensuring that domain experts can understand drivers and limitations of their predictions. Explainability also provides valuable feedback for further model refinement. Specifically, we observe that the model lacks emphasis on internal edges within microcrystals, with the promotion of internal edge features in future iterations of MicroCrystalNet potentially providing improved performance and higher order classification capabilities (esp. through the discrimination of AA vs. SA subclasses).

5.2. Performance Comparison with Baseline Models

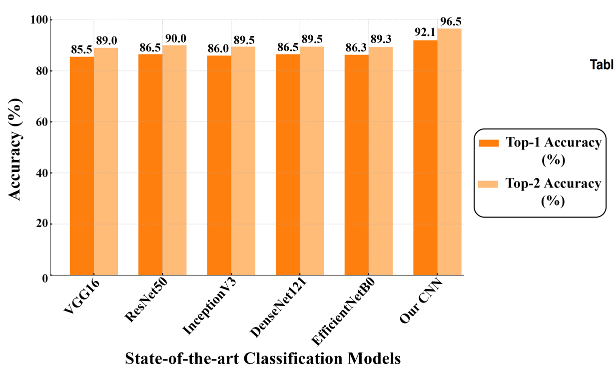

Table 7. Performance comparison of our CNN with state-of-the-art classification models.

Model	Top-1 Accuracy (%)	Top-2 Accuracy (%)	Precision	Recall	F1-Score
VGG16	85.5	89.0	0.860	0.859	0.860
ResNet50	86.5	90.0	0.870	0.869	0.870
InceptionV3	86.0	89.5	0.865	0.864	0.865
DenseNet121	86.5	89.5	0.870	0.869	0.870
EfficientNetB0	86.3	89.3	0.868	0.867	0.868
Our CNN	**92.12**	**96.53**	**0.9139**	**0.9092**	**0.9115**

Figure 10: Model performance comparison to benchmark CNN classifiers.

We compared MicroCrystalNet against five state-of-the-art classification models: VGG16, ResNet50, InceptionV3, DenseNet121, and EfficientNetB0. These models are well-regarded in the deep learning community for their high performance on various benchmark datasets. VGG16 is known for its simplicity and depth, providing a solid baseline. ResNet50 introduces residual connections that help train deeper networks by mitigating the vanishing gradient problem. InceptionV3 employs a complex architecture with inception modules to capture multi-scale features with different kernel sizes. DenseNet121 uses dense connections to improve gradient flow and parameter efficiency. EfficientNetB0, a recent advancement, optimizes the network's depth and width using a compound scaling method.

Comparison against baseline models reveals that MicroCrystalNet maintains competitive performance against these sophisticated architectures whilst being lightweight. Specifically, our model excels in computational efficiency and training speed, making it a viable option for scenarios where computational resources are limited. Despite its simpler architecture, our model achieves high classification accuracy, showcasing its effectiveness for SEM microcrystal form classification.

The proposed CNN demonstrated superior performance to the compared frameworks, achieving an accuracy of 92% (Top-1) and 96.53% (Top-2), a precision of 91.39%, a recall of 90.92%, and an F1-score of 91.15%. In comparison, the baseline models achieved lower performance metrics, with VGG16 achieving an accuracy of 85.5%, ResNet50 at 86.5%, and DenseNet121 at 86.5% (see Figure 10).

Extensive ablation studies were conducted on the model architectures and parameters to identify the optimal model configuration. The detailed results of these ablation studies are presented in the supplementary section.

6. Discussion

Rapid developments in the allied fields of computer vision and artificial intelligence are revolutionizing geo-image processing and analysis, impacting geoscience disciplines employing a broad variety of imaging modalities across manifold scales of observation (e.g., Valentín et al. (2019); Zheng et al. (2019); Han et al. (2022); Jayachandran et al. (2024)). With regards to the segmentation and classification of micron- to nanometric resolution image datasets, such developments have permeated deeply into x-ray microcomputed tomographic image analysis workflows (Ar Rushood et al. (2020); Varfolomeev et al. (2019); dos Anjos et al. (2021)), with workers now employing power generative AI to elicit super-resolution segmentations of conventionally challenging lithotypes (i.e., carbonate rocks with multimodal pore systems:

Alqahtani et al. (2022); Buono et al. (2023); Roslin et al. (2023)). Arguably, the inertia accrued over the past decade within the x-ray micro CT digital rocks community: itself attributable to the amenable nature of x-ray µCT volume images for rock physical property extraction, can be regarded as the key driver of the rapid proliferation of deep learning based image processing within this field. The development of versatile deep learning-based segmentation and classification toolchains to raster datasets generated by scanning electron microscopy has, however, enjoyed comparatively less traction. This relative dearth of implemented frameworks for SEM petrography is perhaps attributable to some of the inherent challenges pertaining to SEM image processing and any subsequent extraction of meaningful rock physical properties. For example, the imposition of scene artifacts (i.e., charging effects, occlusions, perspective distortions) varies widely between samples, dependent upon material composition and degree of sample preparation (i.e., rough cut samples vs. quasi-2D polished surfaces), making the development of a generalizable segmentation pipeline capable of handling challenging edge cases (i.e., rough topographic surfaces) challenging. Moreover, irrespective of sample preparation, stereological effects make the extraction of meaningful rock volume physical properties or the characterization of microtextural fabrics highly non-trivial, with any such analyses resulting in 'apparent' properties subject to considerable skew and orientation bias (e.g., Higgins (1994)).

The ubiquitous nature of SEM imaging in the petrographic analysis of microcrystalline rocks coupled with the challenges such images pose towards conventional image processing and analysis techniques warrants the development of bespoke tools. In this regard, we suggest that SEM image segmentation and classification pipeline presented herein represents a major advancement in the field, providing the capacity to conduct high-volume data analytics of microcrystalline textures and properties upon geological media which has historically been the purview of low throughput manual measurements and heavily descriptive, qualitative analysis. In the context of the current implementation of MicroCrystalNet, which has been trained using an extensive set of Low-Mg calcite microcrystal patches, the availability of such functionality holds major implications for the characterization of microcrystalline carbonate rocks, potentially impacting several economically and scientifically significant application areas (e.g., reservoir and aquifer characterization, paleoenvironmental reconstruction and paragenetic studies etc.). For example, it is common practice within integrated carbonate reservoir characterization to attempt to correlate microcrystalline textures observed in SEM images to petrophysical signatures obtained from core plugs and well bore geophysics (esp. MICP/NMR) / (e.g.: Fleury et al. (2007); Aliakbardoust and Rahimpour-Bonab (2013); Rebelle and Lalanne (2014)), forming the basis for rock typing schemes. Within such workflows, there is a major disconnect in the scale of observation between the SEM image analysis and paired datasets, with the limited coverage offered by SEM petrography at the core plug scale, coupled with the qualitative nature of its analysis meaning that microtextural information is at best anecdotal within carbonate rock typing frameworks. Moreover, a similar lack of representativity and qualitative rigour offered by conventional SEM petrography limits the robustness of paragenetic studies employing SEM petrography to elicit the diagenetic histories of ancient carbonate rocks (e.g., Melim et al. (2002); Rinderknecht et al. (2021)). By providing the capacity for high volume, objective LMC microcrystallometry which considers the spectrum of pertinent calcite morphological properties, the presented framework shifts the emphasis of carbonate microcrystalline characterization towards quantitative and reproducible analytics. In turn, these evolved capabilities offer the potential to forward the role of SEM petrography within carbonate rock typing and paragenetic studies, providing unprecedented data volumes which can both be used to scale up microtextural properties to the core plug / core scale and elicit broad spatiotemporal trends in LMC microcrystal morphometry across manifold scales (i.e., outcrop, reservoir, field and basin scale).

For parsimony, the MicroCrystalNet has been trained using an abridged implementation of the LMC classification scheme shown in Figure 1, demonstrating promising results in distinguishing between these four primary morphological classes (i.e., Rhombic-Euhedral/Subhedral, Polyhedral-Euhedral/ Subhedral, Amorphous-Anhedral and Rounded-Anhedral). However, the model's utility in carbonate rock characterization can be enhanced by extending its classification capabilities to distinguish between subhedral and euhedral classes within both the polyhedral and rhombic crystal shapes. Furthermore, the additional criteria, such as crystal size could be utilized to further refine the classification task, potentially providing insights into the evolution of microcrystalline calcite nucleation and stabilization within a studied system (e.g., Bischoff et al. (1993); Hashim and Kaczmarek (2020)). Beyond the scope of low-Mg calcite microtextures, MicroCrystalNet has the potential to impact SEM petrographic analysis of microcrystalline rock textures presented by a broad range of rock types, encompassing other carbonate lithologies (e.g., dolomitized textures, and high-Mg calcite and aragonitic sediments: Kretz (1988); Hover et al. (2001)) and beyond (e.g., intrusive and volcanic igneous rocks, clastic reservoirs, ore deposits: French and Worden (2013); Wohletz (1983); Egglseder et al. (2019)). In the case of non-porous, crystalline rocks (i.e., intrusive igneous, metamorphic and metalliferous ore samples), SEM petrography is commonly conducted upon polished surfaces, with the resulting micrographs being relatively free of the scene artifacts which pose significant challenges to conventional segmentation routines, and arguably represent more trivial cases for the presented pipeline when compared to the rough topographic surfaces of LMC crystals considered here. Such samples, however, do potentially require more extensive training sets, due to the mapped crystals being more akin to 2D cross sections, whereby multiple angles and stories of intersection are required to fully capture each crystal class's form.

It should be noted that achieving finer granularity in classification, either through the refinement of the current LMC classifier or via expansion into more complex microcrystalline mineral assemblages necessitates the incorporation of additional layers and refined feature extraction techniques to capture subtle differences in facet morphology and/or internal crystalline structure. Furthermore, evaluation against state-of-the-art vision transformers (ViTs) models is essential (e.g., Li et al. (2022)), as ViTs have demonstrated superior performance in capturing global contextual information through self-attention mechanisms, which could potentially outperform traditional CNNs in microcrystal morphometric analysis. The comparative analysis between CNN and ViT models will provide critical insights into the advantages and limitations of each approach in the context of microcrystal classification. Additionally, further exploration of the role of sparse reduction blocks, which aim to reduce computational complexity while preserving essential structural information, is imperative. These blocks can facilitate efficient processing of high-resolution SEM images without significant loss of detail, thereby improving model performance. Integrating advanced deep learning techniques such as residual connections can further enhance the model's ability to generalize across diverse datasets. These multifaceted approaches will not only refine the current classification framework but also pave the way for more sophisticated and nuanced analyses of microcrystal morphometry within petrographic studies.

7. Conclusion

In this work, we have presented a state-state-of-the-art computer vision pipeline based upon deep learning architectures which facilitates the instance segmentation and classification of microcrystals from scanning electron microscopy images. Deployed using SEM images of roughly cleaved low-Mg calcite surfaces, our CNN model for microcrystal classification has demonstrated high performance against state-of-the-art classifiers, offering significant potential for advancing the petrographic study of microcrystalline textures away from subjective, manual interpretation towards high volume, quantitative crystallometry at nanometric scales. In the context of the current application towards carbonate rock characterization, the integration of advanced computer vision and deep learning techniques with traditional petrographic analyses provide a powerful tools, which offer the potential to elicit complex interactions between microcrystal morphologies and their geological and petrophysical contexts. This nascent application is, however, just one example of where automated SEM petrography can profoundly impact the microtextural characterization of geologic media, with our open source framework being potentially transformative towards the study of numerous microcrystalline media, including intrusive and volcanic igneous rocks, clastic reservoirs, and metalliferous ore deposits.

Acknowledgements

The financial assistance of the Qatar National Research Fund (QNRF) through the National Priorities Research Program (Projects: NPRP10-0104-170104 / NPRP12S-0302-190194), as well as industry funding from North Oil Company and Total Energies, is gratefully acknowledged.

Computer Code Availability

The code and software used in this research are available in the following public repository:

- Name: MicroCrystalNet - Advanced Microcrystal Classification Using Normalized Sparse Reduction Blocks

- Version: 1.0

- License: MIT License (https://opensource.org/licenses/MIT)
- Repository: https://github.com/YaqoobAnsari/MicroCrystalNet-Advanced-Microcrystal-Classification-Using-Normalized-Sparse-Reduction-Blocks

The research utilized Python 3.11 and TensorFlow compatible with this version.

No proprietary software or non-open-source code was used in this research.

Author contributions statement

Conceptualization, M.Y.A., and M.Yusuf.A.; Data collection and labeling, M.Y.A., I.S.A.J.J., and M.H.; Formal analysis, M.I.; Methodology, M.Y.A., and M.I.; Supervision, T.D.S.; Validation, M.Y.A., and M.I.; Visualization M.Y.A.; Writing—original draft, M.Y.A., and M.Yusuf.A.; Writing—review & editing, M.Yusuf.A., M.I., and M.H.; Data Curation, T.D.S. All the authors revised and approved the final manuscript.

References

Agarap, A.F., 2018. Deep learning using rectified linear units (relu). arXiv preprint arXiv:1803.08375 .

Aliakbardoust, E., Rahimpour-Bonab, H., 2013. Integration of rock typing methods for carbonate reservoir characterization. Journal of Geophysics and Engineering 10, 055004.

Alqahtani, N.J., Niu, Y., Wang, Y.D., Chung, T., Lanetc, Z., Zhuravljov, A., Armstrong, R.T., Mostaghimi, P., 2022. Super-resolved segmentation of x-ray images of carbonate rocks using deep learning. Transport in Porous Media 143, 497–525.

Andrä, H., Combaret, N., Dvorkin, J., Glatt, E., Han, J., Kabel, M., Keehm, Y., Krzikalla, F., Lee, M., Madonna, C., et al., 2013. Digital rock physics benchmarks—part ii: Computing effective properties. Computers & Geosciences 50, 33–43.

Andrew, M., Bijeljic, B., Blunt, M.J., 2014. Pore-scale contact angle measurements at reservoir conditions using x-ray microtomography. Advances in Water resources 68, 24–31.

dos Anjos, C.E., Avila, M.R., Vasconcelos, A.G., Pereira Neta, A.M., Medeiros, L.C., Evsukoff, A.G., Surmas, R., Landau, L., 2021. Deep learning for lithological classification of carbonate rock micro-ct images. Computational Geosciences 25, 971–983.

Ansari, M.Y., Chandrasekar, V., Singh, A.V., Dakua, S.P., 2022. Re-routing drugs to blood brain barrier: A comprehensive analysis of machine learning approaches with fingerprint amalgamation and data balancing. IEEE Access 11, 9890–9906.

Ansari, M.Y., Qaraqe, M., Charafeddine, F., Serpedin, E., Righetti, R., Qaraqe, K., 2023a. Estimating age and gender from electrocardiogram signals: A comprehensive review of the past decade. Artificial Intelligence in Medicine , 102690.

Ansari, M.Y., Qaraqe, M., Righetti, R., Serpedin, E., Qaraqe, K., 2023b. Unveiling the future of breast cancer assessment: a critical review on generative adversarial networks in elastography ultrasound. Frontiers in Oncology 13, 1282536.

Ansari, M.Y., Qaraqe, M., Righetti, R., Serpedin, E., Qaraqe, K., 2024. Enhancing ecg-based heart age: impact of acquisition parameters and generalization strategies for varying signal morphologies and corruptions. Frontiers in Cardiovascular Medicine 11, 1424585.

Ansari, Y., Tiyal, N., Flushing, E.F., Razak, S., 2021. Prediction of indoor wireless coverage from 3d floor plans using deep convolutional neural networks., in: LCN, pp. 435–438.

Anusree, K., Latha, G.M., 2023. Characterization of sand particle morphology: state-of-the-art. Bulletin of Engineering Geology and the Environment 82, 269.

Ar Rushood, I., Alqahtani, N., Wang, Y.D., Shabaninejad, M., Armstrong, R., Mostaghimi, P., 2020. Segmentation of x-ray images of rocks using deep learning, in: SPE Annual Technical Conference and Exhibition?, SPE. p. D041S042R002.

Baldi, P., Sadowski, P.J., 2013. Understanding dropout. Advances in neural information processing systems 26.

Bischoff, W.D., Bertram, M.A., Mackenzie, F.T., Bishop, F.C., 1993. Diagenetic stabilization pathways of magnesian calcites. Carbonates and Evaporites 8, 82–89.

Bjorck, N., Gomes, C.P., Selman, B., Weinberger, K.Q., 2018. Understanding batch normalization. Advances in neural information processing systems 31.

Blott, S.J., Pye, K., 2008. Particle shape: a review and new methods of characterization and classification. Sedimentology 55, 31–63.

Buono, G., Caliro, S., Macedonio, G., Allocca, V., Gamba, F., Pappalardo, L., 2023. Exploring microstructure and petrophysical properties of microporous volcanic rocks through 3d multiscale and super-resolution imaging. Scientific Reports 13, 6651.

Cantrell, D.L., Hagerty, R.M., et al., 1999. Microporosity in arab formation carbonates, saudi arabia. GeoArabia 4, 129–154.

Cao, Y., Linnen, R., Good, D., Samson, I., 2018. Applications of the combined portable xrf-benchtop sem methodology to pge exploration. Ore Geology Reviews 101, 32–53.

Carpentier, C., Ferry, S., Lécuyer, C., Strasser, A., Géraud, Y., Trouiller, A., 2015. Origin of micropores in late jurassic (oxfordian) micrites of the eastern paris basin, france. Journal of Sedimentary Research 85, 660–682.

Chandrasekar, V., Ansari, M.Y., Singh, A.V., Uddin, S., Prabhu, K.S., Dash, S., Al Khodor, S., Terranegra, A., Avella, M., Dakua, S.P., 2023. Investigating the use of machine learning models to understand the drugs permeability across placenta. IEEE Access 11, 52726–52739.

Cheadle, C., Vawter, M.P., Freed, W.J., Becker, K.G., 2003. Analysis of microarray data using z score transformation. The Journal of molecular diagnostics 5, 73–81.

Chen, W., Du, X., Yang, F., Beyer, L., Zhai, X., Lin, T.Y., Chen, H., Li, J., Song, X., Wang, Z., et al., 2021. A simple single-scale vision transformer for object localization and instance segmentation. arXiv preprint arXiv:2112.09747 .

Christlein, V., Spranger, L., Seuret, M., Nicolaou, A., Král, P., Maier, A., 2019. Deep generalized max pooling, in: 2019 International conference on document analysis and recognition (ICDAR), IEEE. pp. 1090–1096.

Deardorff, N., Cashman, K., 2017. Rapid crystallization during recycling of basaltic andesite tephra: timescales determined by reheating experiments. Scientific reports 7, 46364.

Egglseder, M.S., Cruden, A.R., Tomkins, A.G., Wilson, S., Dalstra, H.J., Rielli, A., Li, C., Baumgartner, J., Faivre, D., 2019. Tiny particles building huge ore deposits–particle-based crystallisation in banded iron formation-hosted iron ore deposits (hamersley province, australia). Ore Geology Reviews 104, 160–174.

Ehrenberg, S.N., Walderhaug, O., Bjorlykke, K., 2012. Carbonate porosity creation by mesogenetic dissolution: reality or illusion? AAPG bulletin 96, 217–233.

Fan, J., Gao, B., Ge, Q., Ran, Y., Zhang, J., Chu, H., 2023. Segtransconv: transformer and cnn hybrid method for real-time semantic segmentation of autonomous vehicles. IEEE Transactions on Intelligent Transportation Systems .

Fleury, M., Santerre, Y., Vincent, B., 2007. Carbonate rock typing from nmr relaxation measurements, in: SPWLA Annual Logging Symposium, SPWLA. pp. SPWLA–2007.

Folk, R.L., 1965. Some aspects of recrystallization in ancient limestones .

Folk, R.L., Robles, R., 1964. Carbonate sands of isla perez, alacran reef complex, yucatan. The Journal of Geology 72, 255–292.

French, M.W., Worden, R.H., 2013. Orientation of microcrystalline quartz in the fontainebleau formation, paris basin and why it preserves porosity. Sedimentary Geology 284, 149–158.

Friedman, G.M., 1965. Occurrence and stability relationships of aragonite, high-magnesian calcite, and low-magnesian calcite under deep-sea conditions. Geological Society of America Bulletin 76, 1191–1196.

Gao, Y., Raeini, A.Q., Selem, A.M., Bondino, I., Blunt, M.J., Bijeljic, B., 2020. Pore-scale imaging with measurement of relative permeability and capillary pressure on the same reservoir sandstone sample under water-wet and mixed-wet conditions. Advances in Water Resources 146, 103786.

Gischler, E., Erkoç, M.M., 2013. Facies of devonian fore reef limestones: a quantitative study (iberg reef, harz mts., germany). Palaeobiodiversity and Palaeoenvironments 93, 91–101.

Godinho, J.R.A., Hassanzadeh, A., Heinig, T., 2023. 3d quantitative mineral characterization of particles using x-ray computed tomography. Natural Resources Research 32, 479–499.

Guntoro, P.I., Ghorbani, Y., Koch, P.H., Rosenkranz, J., 2019. X-ray microcomputed tomography (μct) for mineral characterization: A review of data analysis methods. Minerals 9, 183.

Han, W., Li, J., Wang, S., Zhang, X., Dong, Y., Fan, R., Zhang, X., Wang, L., 2022. Geological remote sensing interpretation using deep learning feature and an adaptive multisource data fusion network. IEEE Transactions on Geoscience and Remote Sensing 60, 1–14.

Hashim, M.S., 2022. Experimental Insights Into The Origin Of Microcrystalline Calcites. Western Michigan University.

Hashim, M.S., Kaczmarek, S.E., 2019. A review of the nature and origin of limestone microporosity. Marine and Petroleum Geology 107, 527–554.

Hashim, M.S., Kaczmarek, S.E., 2020. Experimental stabilization of carbonate sediments to calcite: insights into the depositional and diagenetic controls on calcite microcrystal texture. Earth and Planetary Science Letters 538, 116235.

Hashim, M.S., Kaczmarek, S.E., 2021. Evolution of calcite microcrystal morphology during experimental dissolution. Journal of Sedimentary Research 91, 229–242.

Hasiuk, F.J., Kaczmarek, S.E., Fullmer, S.M., 2016. Diagenetic origins of the calcite microcrystals that host microporosity in limestone reservoirs. Journal of Sedimentary Research 86, 1163–1178.

Hassan, A., Chandra, V., Yutkin, M.P., Patzek, T.W., Espinoza, D., 2019. Imaging and characterization of microporous carbonates using confocal and electron microscopy of epoxy pore casts. SPE Journal 24, 1220–1233.

Higgins, M.D., 1994. Numerical modeling of crystal shapes in thin sections: estimation of crystal habit and true size. American Mineralogist 79, 113–119.

Ho, Y., Wookey, S., 2019. The real-world-weight cross-entropy loss function: Modeling the costs of mislabeling. IEEE access 8, 4806–4813.

Hörst, F., Rempe, M., Heine, L., Seibold, C., Keyl, J., Baldini, G., Ugurel, S., Siveke, J., Grünwald, B., Egger, J., et al., 2024. Cellvit: Vision transformers for precise cell segmentation and classification. Medical Image Analysis 94, 103143.

Hover, V.C., Walter, L.M., Peacor, D.R., 2001. Early marine diagenesis of biogenic aragonite and mg-calcite: new constraints from high-resolution stem and aem analyses of modern platform carbonates. Chemical Geology 175, 221–248.

Hryciw, R.D., Zheng, J., Shetler, K., 2016. Particle roundness and sphericity from images of assemblies by chart estimates and computer methods. Journal of Geotechnical and Geoenvironmental Engineering 142, 04016038.

Huang, Z., Wang, N., 2018. Data-driven sparse structure selection for deep neural networks, in: Proceedings of the European conference on computer vision (ECCV), pp. 304–320.

Jacobs, R., 2022. Deep learning object detection in materials science: Current state and future directions. Computational Materials Science 211, 111527.

Jayachandran, I.S.A.J., Gibbs, H.C., Laya, J.C., Qaiser, Y., Khan, T., Ansari, M.I.M.S., Ansari, M.Y., Malyah, M., Alyafei, N., Seers, T.D., 2024. An object-based approach to differentiate pores and microfractures in petrographic analysis using explainable, supervised machine learning. Earth and Space Science 11, e2023EA003291.

Jouini, M., Vega, S., Mokhtar, E., 2011. Multiscale characterization of pore spaces using multifractals analysis of scanning electronic microscopy images of carbonates. Nonlinear Processes in Geophysics 18, 941–953.

Kaczmarek, S.E., Fullmer, S.M., Hasiuk, F.J., 2015. A universal classification scheme for the microcrystals that host limestone microporosity. Journal of Sedimentary Research 85, 1197–1212.

Kirillov, A., Mintun, E., Ravi, N., Mao, H., Rolland, C., Gustafson, L., Xiao, T., Whitehead, S., Berg, A.C., Lo, W.Y., et al., 2023. Segment anything, in: Proceedings of the IEEE/CVF International Conference on Computer Vision, pp. 4015–4026.

Kong, L., Ostadhassan, M., Hou, X., Mann, M., Li, C., 2019. Microstructure characteristics and fractal analysis of 3d-printed sandstone using micro-ct and sem-eds. Journal of Petroleum Science and Engineering 175, 1039–1048.

Kretz, R., 1988. Sem study of dolomite microcrystals in grenville marble. American Mineralogist 73, 619–631.

Krull, A., Buchholz, T.O., Jug, F., 2019. Noise2void-learning denoising from single noisy images, in: Proceedings of the IEEE/CVF conference on computer vision and pattern recognition, pp. 2129–2137.

Lambert, L., Durlet, C., Loreau, J.P., Marnier, G., 2006. Burial dissolution of micrite in middle east carbonate reservoirs (jurassic–cretaceous): keys for recognition and timing. Marine and Petroleum Geology 23, 79–92.

Lautze, N.C., Taddeucci, J., Andronico, D., Cannata, C., Tornetta, L., Scarlato, P., Houghton, B., Castro, M.D.L., 2012. Sem-based methods for the analysis of basaltic ash from weak explosive activity at etna in 2006 and the 2007 eruptive crisis at stromboli. Physics and Chemistry of the Earth, Parts A/B/C 45, 113–127.

Lee, K., Sung, S.H., Kim, D.h., Park, S.h., 2019. Verification of normalization effects through comparison of cnn models, in: 2019 International Conference on Multimedia Analysis and Pattern Recognition (MAPR), IEEE. pp. 1–5.

Li, Y., Wu, C.Y., Fan, H., Mangalam, K., Xiong, B., Malik, J., Feichtenhofer, C., 2022. Mvitv2: Improved multiscale vision transformers for classification and detection, in: Proceedings of the IEEE/CVF conference on computer vision and pattern recognition, pp. 4804–4814.

Longman, M.W., Mench, P.A., 1978. Diagenesis of cretaceous limestones in the edwards aquifer system of south-central texas: a scanning electron microscope study. Sedimentary Geology 21, 241–276.

Maćkiewicz, A., Ratajczak, W., 1993. Principal components analysis (pca). Computers & Geosciences 19, 303–342.

Mathews, R., 1966. Genesis of recent lime mud in southern british honduras. Journal of Sedimentary Research 36, 428–454.

Melim, L., Westphal, H., Swart, P., Eberli, G., Munnecke, A., 2002. Questioning carbonate diagenetic paradigms: evidence from the neogene of the bahamas. Marine Geology 185, 27–53.

Milliken, K.L., Curtis, M.E., 2016. Imaging pores in sedimentary rocks: Foundation of porosity prediction. Marine and Petroleum Geology 73, 590–608.

Morad, D., Paganoni, M., Al Harthi, A., Morad, S., Ceriani, A., Mansurbeg, H., Al Suwaidi, A., Al-Aasm, I.S., Ehrenberg, S.N., 2018. Origin and evolution of microporosity in packstones and grainstones in a lower cretaceous carbonate reservoir, united arab emirates .

Moshier, S.O., 1989. Microporosity in micritic limestones: a review. Sedimentary geology 63, 191–213.

Norbisrath, J.H., Eberli, G.P., Laurich, B., Desbois, G., Weger, R.J., Urai, J.L., 2015. Electrical and fluid flow properties of carbonate microporosity types from multiscale digital image analysis and mercury injection. AAPG bulletin 99, 2077–2098.

Ogasawara, Y., 2005. Microdiamonds in ultrahigh-pressure metamorphic rocks. Elements 1, 91–96.

Otsu, N., et al., 1975. A threshold selection method from gray-level histograms. Automatica 11, 23–27.

de Periere, M.D., Durlet, C., Vennin, E., Lambert, L., Bourillot, R., Caline, B., Poli, E., 2011. Morphometry of micrite particles in cretaceous microporous limestones of the middle east: Influence on reservoir properties. Marine and Petroleum Geology 28, 1727–1750.

Puskarczyk, E., Krakowska, P., Jędrychowski, M., Habrat, M., Madejski, P., 2018. A novel approach to the quantitative interpretation of petrophysical parameters using nano-ct: example of paleozoic carbonates. Acta Geophysica 66, 1453–1461.

Rai, P., Ansari, M.Y., Warfa, M., Al-Hamar, H., Abinahed, J., Barah, A., Dakua, S.P., Balakrishnan, S., 2023. Efficacy of fusion imaging for immediate post-ablation assessment of malignant liver neoplasms: A systematic review. Cancer Medicine 12, 14225–14251.

Rebelle, M., Lalanne, B., 2014. Rock-typing in carbonates: A critical review of clustering methods, in: Abu Dhabi international petroleum exhibition and conference, SPE. p. D041S070R002.

Regnet, J., David, C., Fortin, J., Robion, P., Makhloufi, Y., Collin, P.Y., 2015. Influence of microporosity distribution on the mechanical behavior of oolithic carbonate rocks. Geomechanics for Energy and the Environment 3, 11–23.

Regnet, J., David, C., Robion, P., Menéndez, B., 2019. Microstructures and physical properties in carbonate rocks: A comprehensive review. Marine and Petroleum Geology 103, 366–376.

Richard, J., Sizun, J.P., Machhour, L., 2007. Development and compartmentalization of chalky carbonate reservoirs: the urgonian jura-bas dauphine platform model (genissiat, southeastern france). Sedimentary Geology 198, 195–207.

Rinderknecht, C.J., Hasiuk, F.J., Oborny, S.C., 2021. Mg zonation and heterogeneity in low-mg calcite microcrystals of a depositional chalk. Journal of Sedimentary Research 91, 795–811.

Roduit, N., et al., 2007. JMicroVision: un logiciel d'analyse d'images pétrographiques polyvalent. volume 65. Section des Sciences de la Terre, Université de Genève.

Roslin, A., Marsh, M., Provencher, B., Mitchell, T., Onederra, I., Leonardi, C., 2023. Processing of micro-ct images of granodiorite rock samples using convolutional neural networks (cnn), part ii: Semantic segmentation using a 2.5 d cnn. Minerals Engineering 195, 108027.

Schindelin, J., Rueden, C.T., Hiner, M.C., Eliceiri, K.W., 2015. The imagej ecosystem: An open platform for biomedical image analysis. Molecular reproduction and development 82, 518–529.

Schmidt, M., Fung, G., Rosales, R., 2007. Fast optimization methods for l1 regularization: A comparative study and two new approaches, in: Machine Learning: ECML 2007: 18th European Conference on Machine Learning, Warsaw, Poland, September 17-21, 2007. Proceedings 18, Springer. pp. 286–297.

Sharma, N., Jain, V., Mishra, A., 2018. An analysis of convolutional neural networks for image classification. Procedia computer science 132, 377–384.

Siddique, A., Godinho, J.R., Sittner, J., Pereira, L., 2023. Overcoming stereological bias: A workflow for 3d mineral characterization of particles using x-ray micro-computed tomography. Minerals Engineering 201, 108200.

Smodej, J., Reuning, L., Becker, S., Kukla, P.A., 2019. Micro-and nanopores in intrasalt, microbialite-dominated carbonate reservoirs, ara group, south-oman salt basin. Marine and Petroleum Geology 104, 389–403.

Sok, R.M., Knackstedt, M.A., Varslot, T., Ghous, A., Latham, S., Sheppard, A.P., 2010. Pore scale characterization of carbonates at multiple scales: Integration of micro-ct, bsem, and fibsem. Petrophysics-The SPWLA Journal of Formation Evaluation and Reservoir Description 51.

Steinen, R.P., 1979. On the diagenesis of lime mud: Scanning electron microscopic observations of subsurface material from barbados, wi: Reply. Journal of Sedimentary Research 49.

Steinen, R.P., 1982. Sem observations on the replacement of bahaman aragonitic mud by calcite. Geology 10, 471–475.

Stripp, G., Field, M., Schumacher, J., Sparks, R., Cressey, G., 2006. Post-emplacement serpentinization and related hydrothermal metamorphism in a kimberlite from venetia, south africa. Journal of Metamorphic Geology 24, 515–534.

Sutha, J., et al., 2020. Object based classification of high resolution remote sensing image using hrsvm-cnn classifier. European Journal of Remote Sensing 53, 16–30.

Tavakoli, V., Jamalian, A., 2018. Microporosity evolution in iranian reservoirs, dalan and dariyan formations, the central persian gulf. Journal of Natural Gas Science and Engineering 52, 155–165.

Trujillo-Pino, A., Krissian, K., Alemán-Flores, M., Santana-Cedrés, D., 2013. Accurate subpixel edge location based on partial area effect. Image and vision computing 31, 72–90.

Valencia, F.L., Laya, J.C., 2020. Deep-burial dissolution in an oligocene-miocene giant carbonate reservoir (perla limestone), gulf of venezuela basin: Implications on microporosity development. Marine and Petroleum Geology 113, 104144.

Valentín, M.B., Bom, C.R., Coelho, J.M., Correia, M.D., De Albuquerque, M.P., de Albuquerque, M.P., Faria, E.L., 2019. A deep residual convolutional neural network for automatic lithological facies identification in brazilian pre-salt oilfield wellbore image logs. Journal of Petroleum Science and Engineering 179, 474–503.

Varfolomeev, I., Yakimchuk, I., Safonov, I., 2019. An application of deep neural networks for segmentation of microtomographic images of rock samples. Computers 8, 72.

Vilcáez, J., Morad, S., Shikazono, N., 2017. Pore-scale simulation of transport properties of carbonate rocks using fib-sem 3d microstructure: Implications for field scale solute transport simulations. Journal of Natural Gas Science and Engineering 42, 13–22.

Vincent, B., Fleury, M., Santerre, Y., Brigaud, B., 2011. Nmr relaxation of neritic carbonates: An integrated petrophysical and petrographical approach. Journal of Applied Geophysics 74, 38–58.

Weng, X., Li, H., Song, S., Liu, Y., 2017. Reducing the entrainment of gangue fines in low grade microcrystalline graphite ore flotation using multi-stage grinding-flotation process. Minerals 7, 38.

Wohletz, K.H., 1983. Mechanisms of hydrovolcanic pyroclast formation: grain-size, scanning electron microscopy, and experimental studies. Journal of Volcanology and Geothermal Research 17, 31–63.

Yang, S., Wang, X., Li, Y., Fang, Y., Fang, J., Liu, W., Zhao, X., Shan, Y., 2022. Temporally efficient vision transformer for video instance segmentation, in: Proceedings of the IEEE/CVF conference on computer vision and pattern recognition, pp. 2885–2895.

Zhang, W., Tang, P., Zhao, L., 2019. Remote sensing image scene classification using cnn-capsnet. Remote Sensing 11, 494.

Zhao, W., Du, S., 2016. Spectral–spatial feature extraction for hyperspectral image classification: A dimension reduction and deep learning approach. IEEE Transactions on Geoscience and Remote Sensing 54, 4544–4554.

Zheng, Y., Zhang, Q., Yusifov, A., Shi, Y., 2019. Applications of supervised deep learning for seismic interpretation and inversion. The Leading Edge 38, 526–533.

Zhong, X., Gallagher, B., Eves, K., Robertson, E., Mundhenk, T.N., Han, T.Y.J., 2021. A study of real-world micrograph data quality and machine learning model robustness. npj Computational Materials 7, 161.